Renal reabsorption in 3D vascularized proximal tubule models

Neil Y. C. Lin[a,b,c], Kimberly A. Homan[a,b], Sanlin S. Robinson[a,b], David B. Kolesky[a,b], Nathan Duarte[a,b], Annie Moisan[c,1], and Jennifer A. Lewis[a,b,1]

[a]Wyss Institute for Biologically Inspired Engineering, Harvard University, Boston, MA 02115; [b]Harvard John A. Paulson School of Engineering and Applied Sciences, Harvard University, Cambridge, MA 02138; and [c]Roche Pharma Research and Early Development, Roche Innovation Center Basel, CH-4070 Basel, Switzerland

Contributed by Jennifer A. Lewis, January 21, 2019 (sent for review September 4, 2018; reviewed by Ondine Cleaver and Ying Zheng)

Three-dimensional renal tissues that emulate the cellular composition, geometry, and function of native kidney tissue would enable fundamental studies of filtration and reabsorption. Here, we have created 3D vascularized proximal tubule models composed of adjacent conduits that are lined with confluent epithelium and endothelium, embedded in a permeable ECM, and independently addressed using a closed-loop perfusion system to investigate renal reabsorption. Our 3D kidney tissue allows for coculture of proximal tubule epithelium and vascular endothelium that exhibits active reabsorption via tubular–vascular exchange of solutes akin to native kidney tissue. Using this model, both albumin uptake and glucose reabsorption are quantified as a function of time. Epithelium–endothelium cross-talk is further studied by exposing proximal tubule cells to hyperglycemic conditions and monitoring endothelial cell dysfunction. This diseased state can be rescued by administering a glucose transport inhibitor. Our 3D kidney tissue provides a platform for in vitro studies of kidney function, disease modeling, and pharmacology.

kidney tissue | proximal tubule | reabsorption | bioprinting | vasculature

Human kidneys filter and reabsorb solutes from roughly 180 L of blood each day (1), making them highly susceptible to damage from drugs (2), toxins (2, 3), and blood-borne diseases (4). The ability to fabricate key components of the nephron, namely the convoluted proximal tubule and surrounding peritubular capillary network, that actively reabsorb solutes from the filtrate would represent an enabling advance in kidney tissue engineering. In vivo proximal tubule (PT) segments reabsorb nearly 100% of glucose, albumin (5), phosphate, amino acids, and other organic solutes as well as 65 to 80% of filtered sodium and water, which are then transported through the ECM to the bloodstream (1). To date, both microfluidic (3, 6–9) and bioprinted (10) PT models have been introduced. Compared with traditional 2D cell culture, these PT models exhibit substantially improved cell morphology (10), expression of key transporters (8, 10), metabolic activity (6), and reduced expression of cell injury markers (7), with the most pronounced improvements reported for 3D bioprinted PTs (10). However, our original 3D PT model lacked vasculature, which limits its utility for renal reabsorption studies.

Here, we report the bioprinting and perfusion of a 3D vascularized PT (3D VasPT) human tissue that exhibits renal reabsorption via tubular–vascular exchange (i.e., cross-talk between a colocalized epithelium and endothelium). To create 3D VasPT models, we first had to modify our original ECM and fugitive ink, reported previously (10), to achieve rapid epithelial cell confluency. Selective and sustained reabsorption is achieved by printing colocalized vascular and proximal tubular channels and then encapsulating them within a highly permeable, engineered ECM. During long-term perfusion, PT epithelial cells (PTECs) within the confluent epithelium exhibit a pronounced enhancement in their microvilli length and density. When fluorescently labeled albumin and inulin are perfused together through the PT, albumin is selectively reabsorbed. Quantitative measurements of glucose reabsorption rates allow direct comparison with reported in vivo values. Finally, by inducing hyperglycemic conditions, we demonstrated that our 3D VasPT model provides a unique platform for exploring interactions relevant for diseases, such as diabetes (11, 12).

Harnessing our multimaterial bioprinting platform (10, 13, 14), we fabricated engineered kidney tissues following the procedure highlighted in Fig. 1*A*. First, a base layer of a modified ECM composed of gelatin and fibrin (10, 13) is deposited on the chip. Upon decreasing the gelatin-to-fibrin ratio from 7.5 to 0.4, we observed more than a fourfold reduction in the time required to achieve a confluent epithelium compared with PTs embedded in our original ECM (10) (*SI Appendix*, Fig. S1) (i.e., from ∼21 d to 3 to 5 d). Using the modified ECM, PTEC confluency is also achieved in serum-free media conditions. Before enzymatic cross-linking, the modified ECM solution possesses a much lower viscosity (∼10-fold) (*SI Appendix*, Fig. S2) and osmolality compared with the original ECM solution (10). As a consequence, the original fugitive ink had to be modified to suppress viscous fingering at the interface between the printed features and the modified ECM (*SI Appendix*, Figs. S2 and S3). Specifically, we added high-molecular-weight poly(ethylene oxide) (PEO; 8×10^7 g/mol) to our original PEO-poly(propylene)-PEO (Pluronic) ink. Similar to the original ink, the modified ink can be removed from the fabricated tissue upon cooling to roughly 4 °C, where it undergoes a gel-to-fluid transition. While this modified ink exhibited rheological properties similar to those of the original fugitive ink (10), it ensures that smooth printed features are retained after encapsulation within the modified ECM (*SI Appendix*, Figs. S2 and S3). Next, we printed several 3D VasPT architectures (Fig. 1*B*), ranging from straight channels to biomimetic designs of increasing complexity (i.e., convoluted PTs with colocalized vasculature printed in- and out-of-plane). Open lumens corresponding to the PT and

Significance

Current kidney-on-chip models lack the 3D geometry, complexity, and functionality vital for recapitulating in vivo renal tissue. We report the fabrication and perfusion of 3D vascularized proximal tubules embedded within an engineered ECM that exhibit active reabsorption of solutes via tubular–vascular exchange. Using this model, we quantified albumin and glucose reabsorption over time. We also studied hyperglycemic effects in the absence and presence of a glucose transport inhibitor. Our 3D kidney tissue provides a platform for in vitro studies of kidney function, disease modeling, and pharmacology.

Author contributions: N.Y.C.L., K.A.H., D.B.K., A.M., and J.A.L. designed research; N.Y.C.L., K.A.H., S.S.R., D.B.K., and N.D. performed research; N.Y.C.L., K.A.H., and A.M. analyzed data; and N.Y.C.L., K.A.H., A.M., and J.A.L. wrote the paper.

Reviewers: O.C., The University of Texas Southwestern Medical Center; and Y.Z., University of Washington.

Conflict of interest statement: The authors have filed a patent on this work. A.M. is an employee of Roche Pharmaceutical company and J.A.L. is a cofounder of Voxel8, Inc.

[1]To whom correspondence may be addressed. Email: annie.moisan@roche.com or jalewis@seas.harvard.edu.

This article contains supporting information online at www.pnas.org/lookup/suppl/doi:10.1073/pnas.1815208116/-/DCSupplemental.

Published online March 4, 2019.

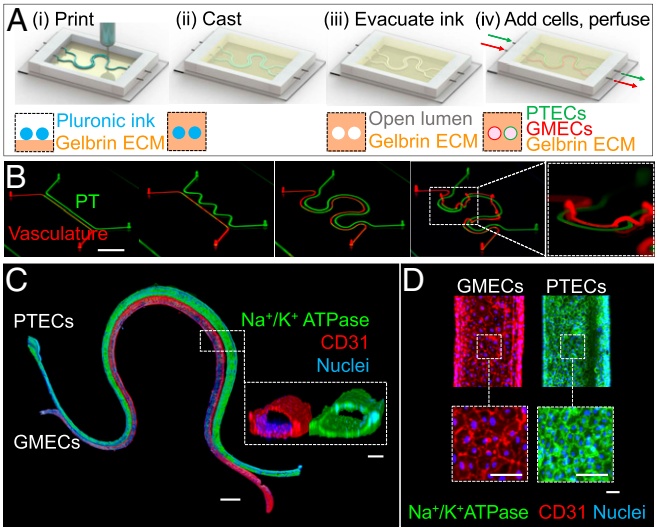

Fig. 1. Design and fabrication of 3D VasPT models. (*A*) Schematic view of 3D VasPT fabrication process. (*B*) Simple and complex 3D VasPT models can be rapidly designed and fabricated. (Scale bar: 10 mm.) (*C*) Whole-mount immunofluorescence staining of the 3D tissue, in which Na^+/K^+ ATPase, CD31, and nuclei (NucBlue staining) are denoted by green, red, and blue, respectively. (Scale bar: 1 mm.) Note: The separation distance between the PT and vascular conduits is ∼70 μm. (*Inset*) Cross-sectional images of the two open lumens. (Scale bars: 100 μm.) (*D*) High-magnification images of 3D VasPT tissue after staining. (Scale bars: 100 μm.)

vascular channels are produced by cooling the chips to 4 °C to liquify and remove the modified fugitive ink. Since the modified ECM has a solute diffusivity roughly 95% of pure water (*SI Appendix*, Fig. S4), vectorial transport between these adjacent channels is readily facilitated.

The fabrication of a representative 3D VasPT chip composed of colocalized convoluted PT and vascular channels is shown in Movie S1. Upon removing the fugitive ink, the PT and vascular channels are seeded with PTECs and vascular endothelial cells, respectively. Specifically, the PT channels are seeded with PTEC-TERT1 cells, which are immortalized through stable expression of the catalytic subunit of human telomerase reverse transcriptase (TERT) (15, 16). These PTECs retain the functional properties of primary cells while maintaining consistent expression levels of functional markers over several passages (16). The vascular channels are seeded with glomerular microvascular endothelial cells (GMECs), which have been widely used in studies of vasculature-related renal disease and nephrotoxicity (17–19). To validate the media conditions and cell compatibility in our PTEC–GMEC coculture, we carried out a series of proliferation assays (*SI Appendix*, Fig. S5). A 3D rendering of the convoluted 3D VasPT tissue obtained by confocal microscopy shows that PTECs and GMECs adhere to the modified ECM and grow to confluency within 3 to 5 d (Fig. 1*C*). A cross-section view of the 3D VasPT tissue reveals the colocalized lumens (∼70-μm separation distance) circumscribed by these respective cell monolayers. Higher-magnification images of each confluent monolayer are shown in Fig. 1*D*.

The ability of our 3D VasPT tissue to recapitulate renal reabsorption depends strongly on cell function and maturity. The PTECs exhibit the appropriate cell polarity, as indicated by basolateral localization of Na^+/K^+ ATPase, apically expressed sodium-glucose cotransporter-2 (SGLT2), and basal-side deposition of basement membrane protein (laminin) (Fig. 2 *A*–*C*). Primary cilia labeled by acetylated tubulin are observed on the apical surface of each PTEC (Fig. 2*D*) (3). Their microvilli density and height (Fig. 2 *E* and *F*) are also significantly higher than PTECs cultured in 2D static conditions (*SI Appendix*, Fig. S6) (10). Consistent with prior work (10), the modified ECM, lumen geometry, and fluidic shear stress used in our 3D VasPT model notably enhance PTEC maturity over time in vitro (*SI Appendix*, Fig. S6), leading to well-established barrier properties (*SI Appendix*, Fig. S7). In addition, we find that the channel diameter increases slightly by ∼10 μm over the first week of culture. As PTECs become more mature, ECM remodeling decreases and their luminal diameter remains constant. This finding along with the laminin deposition (Fig. 2*C*) suggests that PTECs are able to remodel our engineering gelatin–fibrin ECM.

Similar to PTECs, we observe a healthy GMEC phenotype in our 3D VasPT model. For instance, the endothelial marker and intercellular junction protein CD31 is primarily localized at GMEC cell junctions (Figs. 1*D* and 2 *G* and *H*) and expression of the von Willebrand factor (vWF) glycoprotein further confirms their endothelial nature (Fig. 2*H*) (20, 21). We characterized their ultrastructure by transmission electron microscopy (TEM) and observed the formation of adherent junctions (Fig. 2*I*). We also found localization of glycocalyx on their lumnal surface, which appears dark (stained with ruthenium red) in the TEM image shown in Fig. 2*J*. This negatively charged glycoprotein layer is important for flow- and mechano-sensation, interaction with leukocytes, and coagulation (22, 23). Finally, caveolae are observed, which help

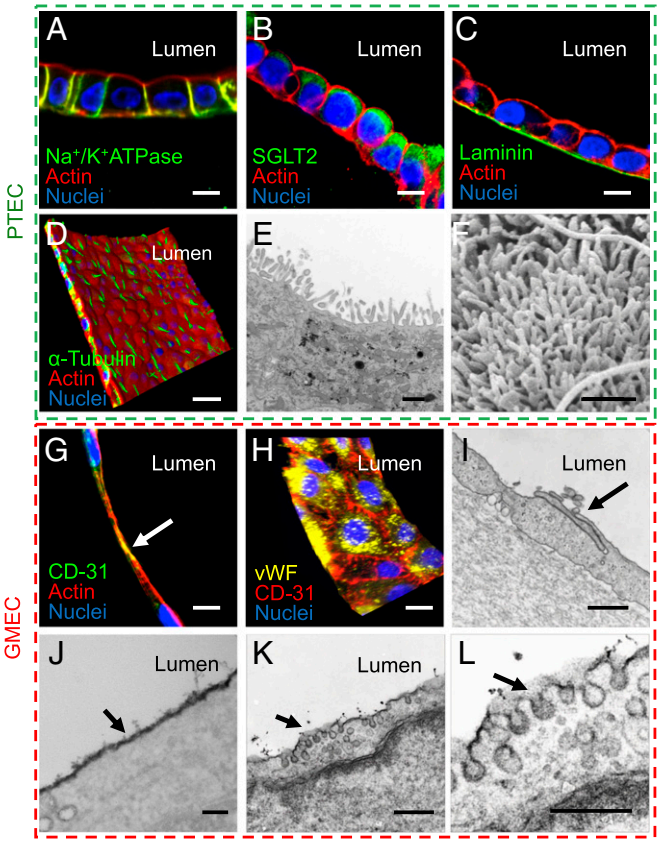

Fig. 2. PTECs and GMECs seeded in 3D VasPT tissues exhibit healthy and mature phenotypes. (*A*–*D*) Fluorescence images of PTECs showing (*A*) Na^+/K^+ ATPase expression primarily located on the basolateral side (green) (Scale bar: 10 μm.); (*B*) apical expression of glucose transporter SGLT2 (green) (Scale bar: 10 μm.); (*C*) deposition of the basement membrane laminin (green) (Scale bar: 10 μm.); and (*D*) primary cilia labeled by α-tubulin (green). (Scale bar: 10 μm.) Red, cytoskeleton labeled by F-actin staining; blue, nuclei labeled by DNA staining. (*E* and *F*) TEM (*E*) and SEM (*F*) micrographs showing densely packed PTEC microvilli that are ∼1.2 μm in height. (Scale bar = 1 μm.) (*G* and *H*) Fluorescence images of GMECs showing (*G*) expression of CD31 (green) predominantly localizes at the GMEC cell–cell junction (arrow) (Scale bar: 10 μm.) and (*H*) granule-like structure of vWF (green) expression in GMECs. (Scale bar: 10 μm.) Red, cytoskeleton labeled by F-actin staining (in *G*); blue, nuclei labeled by DNA staining. (*I*–*L*) TEM images of GMEC (*I*) cell junction, (*J*) glycocalyx, and (*K* and *L*) caveolae-mediated transport. (Scale bars: 1 μm.)

mediate transport across endothelial cell barriers and regulate cell signaling (Fig. 2 *K* and *L*) (24).

To understand coculture effects on cell function, we performed gene expression analysis on the PTEC lysate isolated from our 3D VasPT tissue. In the presence of GMECs, there is an up-regulation of the water transport channel, Aquaporin 1, and the glucose transporter, SGLT2 (*SI Appendix*, Fig. S8). The proliferation marker Ki-67 is also down-regulated, potentially indicative of enhanced PTEC maturity. These findings suggest that positive cross-talk occurs between epithelium and endothelium-lined channels within these 3D tissues. Our observation is in good accord with prior observations (25), that is, endothelial cells secrete multiple factors, such as α-2-macroglobulin antiprotease, that improve PTEC marker gene expression and enzyme activity in coculture experiments.

To demonstrate active reabsorption, we integrated our 3D VasPT model with a closed-loop perfusion system (Fig. 3*A*) that enables tubular and vascular lumens to be individually addressed, specific solutes and drugs to be circulated, and perfusates to be collected at intermittent time points during live imaging. Specifically, we carried out quantitative measurements of albumin and glucose reabsorption, since both solutes play an important role in renal physiology (26, 27). We first measured albumin uptake by perfusing Cy5-conjugated human serum albumin (HSA-Cy5) and inulin-FITC through the PT. HSA-Cy5 is readily reabsorbed by PTECs via receptor-mediated endocytosis. By contrast, inulin-FITC is known to have minimal interaction with these cells, and, hence, serves as a marker for barrier function (28). We measured the concentration of both albumin and inulin-FITC in perfusate samples collected separately from the PT and vascular outlets. After 1 h of exposure to albumin and inulin, we observed significant albumin transport from the PT to the vascular lumen, consistent with the timescale of endocytosis (1) (Fig. 3*B*). While the albumin uptake increases over time, inulin-FITC concentration remains largely unchanged in the PT throughout the experiment, indicative of selective reabsorption. To further evaluate albumin uptake in conditions of high and low cellular activity, we lowered the 3D VasPT tissue temperature to 25 °C, to reduce cellular metabolism. As expected, the albumin uptake decreased by ∼50% under these conditions. Next, we used fluorescence microscopy to directly visualize vectorial transport between the PT and vasculature within the 3D tissue (Fig. 3*C*). Consistent with our quantitative measurements, the HSA-Cy5 is uniformly distributed within the surrounding ECM, whereas inulin-FITC is predominantly confined to the PT lumen (Fig. 3*C*). We also measured the HSA gradient that arises across the PT and vasculature as a function of their relative proximity to one another. We find that the HSA gradient is roughly inversely proportional to the separation distance between channels (*SI Appendix*, Fig. S9).

Healthy kidneys filter 25 to 200 g glucose daily and virtually all of it is reabsorbed (1). To probe glucose reabsorption, we directly measured the difference in glucose concentration between PTEC and GMEC perfusates within our 3D VasPT tissues using a commercial glucose meter (Fig. 3*A*). During each media change, the glucose levels in the PT and vasculature are reset to their initial values of ∼100 mg/dL. The calibration curve and raw data are reported in *SI Appendix*, Fig. S10. Negligible glucose reabsorption is measured for controls composed of either empty (no cells) PT and vascular channels or an empty PT alongside a vascular channel lined with endothelium (Fig. 4*A*). By contrast, epithelialized 3D VasPT tissues with either empty or endothelium-lined vascular channels exhibit similarly high glucose reabsorption levels (Fig. 4*A*), highlighting the crucial role of PTECs in this process. As a final control, we measured glucose reabsorption in transwell experiments, in which PTECs and GMECs are seeded directly onto the membrane or onto membranes precoated with our modified ECM. We find that our 3D VasPT tissues exhibited nearly a 5- to 10-fold enhancement in glucose reabsorption compared with these 2D controls (Fig. 4*B*). The enhanced reabsorption observed in the 3D model is consistent with our prior work (10), in which both luminal architecture and fluidic shear stress were shown to substantially improve PTEC morphology (i.e., cell height and brush border density and length) as well as albumin uptake relative to 2D controls.

To further investigate glucose reabsorption in our 3D VasPT model, we measured the reabsorption rate starting from the day

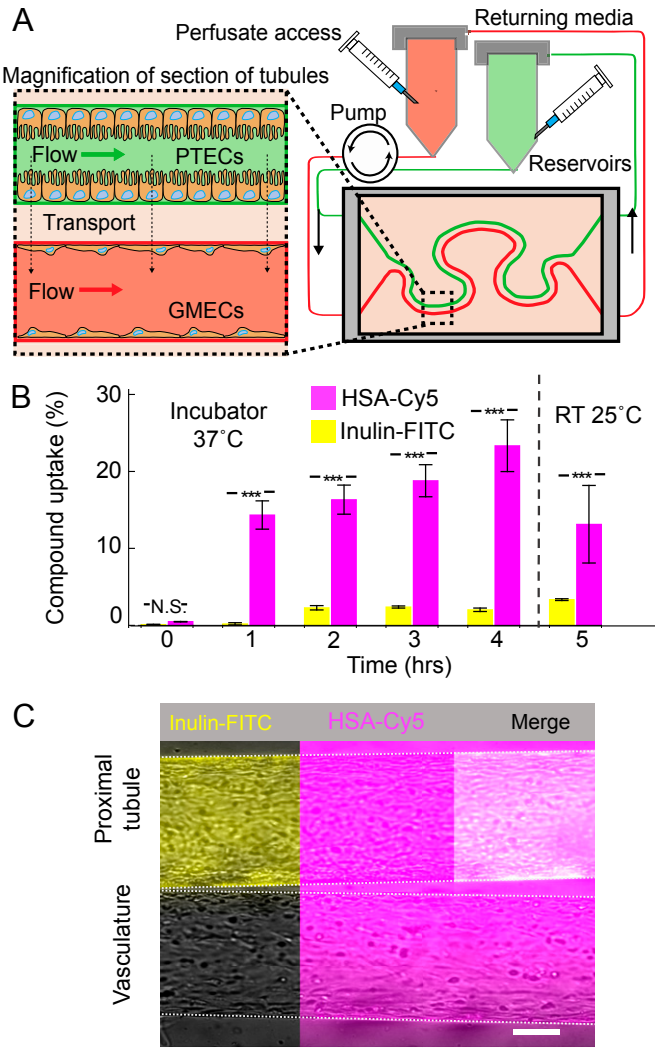

Fig. 3. Albumin reabsorption. (*A*) Integration of 3D VasPT tissue with a closed-loop perfusion system that allows quantitative measurements of renal reabsorption. (*B*) Time evolution of uptake of Cy5-conjugated human serum albumin (HSA-Cy5, purple) and FITC-conjugated inulin (inulin-FITC, yellow). Error bars represent SD of the mean; $n = 3$; N.S., not significant; $^{***}P < 0.0001$. (*C*) Confocal image of colocalized PT and vascular channels (denoted by white dashed lines to guide the eye) that shows PT barrier function and selective transport of HSA-Cy5 from the PTEC to the GMEC channel (purple). (Scale bar: 100 μm.) In this experiment, we acquired images using a fluorescence microscope, which averages the signal intensity within ±1 mm along the vertical direction. Hence, unlike the confocal image provided in *SI Appendix*, Fig. S9, the HSA-Cy5 concentration gradient between PT and vasculature is not readily observed.

PTECs reached full confluency (denoted as day 1) through day 13 (green region, Fig. 4*C*). We find that glucose reabsorption increased over time before reaching a steady-state value of ∼11 μg glucose/mm^2 on day 8. Not surprisingly, this timescale correlates well with the development of a mature brush border (*SI Appendix*, Fig. S6). On day 13, we administered dapagliflozin, which is a known SGLT2 inhibitor, through the PT channel (29). Dapagliflozin is known to bind to and selectively inhibit SGLT2 receptors that are localized at the surface of renal tubular cells. The introduction of this drug led to a pronounced reduction (∼98%) in the glucose reabsorption rate during days 14–15 (red region in Fig. 4*C*), indicating that the glucose reabsorption pathway in these engineered kidney tissues is highly specific and can be regulated (30). This observation is not surprising given that the PTECs are isolated from the S1 segment of human PT, where SGLT2 is the dominant transporter (31). To further validate

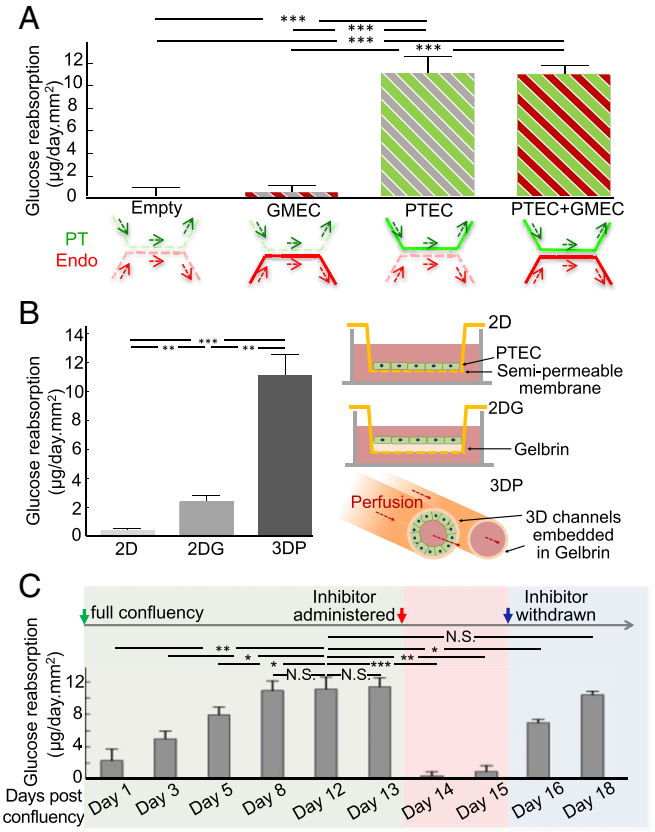

Fig. 4. Glucose reabsorption. (*A*) Quantitative measurements of glucose transport in samples with four different cell seeding configurations showing glucose reabsorption function by PTECs mainly ($n = 4$). (*B*) The physiological microenvironment in our 3D vas-PT tissue substantially enhances the glucose reabsorption efficiency ($n = 4$). (*C*) The reabsorption rate of glucose increases with increasing PTEC maturity (days 1–8, green-gray shading). Upon administration of the SGLT2 inhibitor dapagliflozin, glucose reabsorption was significantly inhibited (days 14–15, red shading). The reabsorption was then gradually restored after dapagliflozin was withdrawn (day 16–18, blue-gray shading). $n = 8$. For all panels, error bars represent SD of the mean, N.S., not significant; $^{*}P < 0.05$; $^{**}P < 0.001$; $^{***}P < 0.0001$.

this finding, we confirmed that SGLT1 gene expression is absent (*SI Appendix*, Fig. S8). Upon withdrawing dapaglifozin on day 15, the glucose reabsorption rate is gradually restored (blue region in Fig. 4*C*). We hypothesize that incomplete restoration of the glucose reabsorption on day 16 is due to the presence of residual dapagliflozin in the system, which appears to be eliminated by day 18. Overall, this multiweek experiment highlights the utility of our 3D VasPT model for longitudinal studies of drug response.

Importantly, we can directly compare the reabsorption efficiency of PTECs within our engineered kidney tissues to their in vivo counterparts. We estimate that PTECs are ∼20% as efficient in reabsorbing glucose in our 3D VasPT model as healthy human kidneys, which reclaim ∼60 μg glucose/mm^2 per day (1). Note that their reabsorption rates are estimated using the PT length, diameter, and measured glucose concentration difference between the two channels in our model. The reabsorptive properties of our engineered kidney tissues may be improved by reducing the PT lumen diameter as well as the separation distance between the PT and vascular conduits. Use of more complex 3D VasPT models, such as those with vascular channels that wrap in and out of plane (Movie S2), may further enhance active reabsorption.

Reabsorption is also implicated in kidney disease. Hyperglycemia is a hallmark of diabetes and a known risk factor for vascular disease (32). Our 3D VasPT model provides a well-characterized platform for probing the effects of hyperglycemia on cell function. To elucidate these effects, we circulated a perfusate with a fourfold higher glucose level (400 mg glucose/dL) than the control sample through the PT (Fig. 5 *A*–*E*). After 36 h of perfusion, we assessed the damage to the endothelial cells induced by these conditions (Fig. 5 *F*–*J*). The GMECs exhibited oxidative stress under hyperglycemic conditions, as indicated by the elevated intensity of CellROX (Fig. 5*G*) and nitrotyrosine (Fig. 5*H*) (33–35). As shown in the TEM images of GMEC ultrastructure (Fig. 5*I*), we also observed disruption of cell–cell junctions due to hyperglycemia. Endothelial dysfunction is accompanied by an up-regulation of VEGF uptake (*SI Appendix*, Fig. S11) (12). Importantly, endothelial function is restored when dapagliflozin is administered (Fig. 5 *K*–*O*), which inhibits glucose transport from the PT to the vasculature, effectively providing a barrier that protects the endothelium from exposure to excess glucose (*SI Appendix*, Fig. S12). We characterized the PTEC morphology under three conditions [hyperglycemic conditions (400 mg glucose/dL) with and without dapagliflozin as well as a control condition (100 mg glucose/dL)]. While the glucose reabsorption rate is up-regulated under hyperglycemia conditions (*SI Appendix*, Fig. S12*A*), we find that the PTEC height is ∼50% lower than that of either the control or the hyperglycemic condition with dapagliflozin (Fig. 5 *E*, *J*, and O). Although these experiments focused on acute glucotoxicity, we believe that longitudinal studies carried out under conditions that mimic chronic hyperglycemia may provide valuable insights into treatments of diabetic vascular diseases.

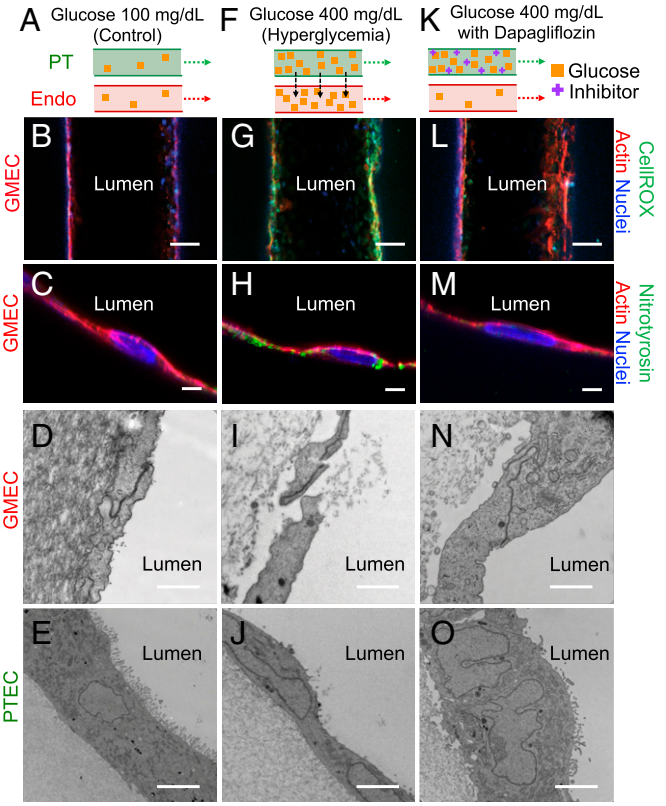

Fig. 5. Hyperglycemic effects. Schematics and cell images of three experimental conditions: (*A*–*E*) normal (control), (*F*–*J*) hyperglycemic, and (*K*–*O*) hyperglycemic with dapagliflozin administered. To generate the hyperglycemic condition, 400 mg/dL glucose is delivered through the PT channel. (*B*, *G*, and *L*) Confocal images of live GMECs incubated with CellROX for reactive oxygen species (ROS) detection (green) under different conditions. (Scale bars: 100 μm.) (*C*, *H*, and *M*) Nitrotyrosine staining of GMECs (green) indicative of ROS/reactive nitrogen species production. (Scale bars: 1 μm.) Red, cytoskeleton; blue, nuclei. (*D*, *I*, and *N*) TEM images of the junctions between GMECs within the confluent endothelium under different conditions. (Scale bar: 1 μm.) (*E*, *J*, and *O*) TEM images of the PTECs within the confluent epithelium under different conditions. (Scale bar: 10 μm.)

In summary, we have created 3D VasPTs that exhibit selective reabsorption and vectorial transport of solutes. The desired renal function is achieved by integrating three crucial components: adjacent open lumens embedded within a permeable ECM, confluent endothelium and epithelium that circumscribe these lumens, and a closed-loop perfusion system that enhances cell maturity and enables controlled introduction of solute species and drugs. We showed that the design and functionality of our model allow for investigative studies of endothelium–epithelium cross-talk under homeostasis and disease conditions. More broadly, our 3D biomanufacturing platform opens new avenues for fabricating vascularized organ-specific tissues for in vitro, and, ultimately, in vivo applications.

Methods

Materials. The modified ECM solution is prepared by mixing together constituents at 37 °C to achieve a final concentration of 1 wt % gelatin, 25 mg/mL fibrinogen, 2.5 mM $CaCl_2$, and 0.2 wt % transglutaminase (TG). Specifically, a 15 wt %/vol % gelatin solution (type A, 300 bloom from porcine skin; Sigma) is produced by warming in DPBS (1× Dulbecco's PBS without calcium and magnesium) to 70 °C and then adding gelatin powder to the solution while vigorously stirring for 12 h at 70 °C. Next, the pH is adjusted to 7.5 adding 1 M NaOH dropwise. The warm gelatin solution is sterile-filtered and stored at 4 °C in aliquots for later use (<3 mo). Fibrinogen solution (80 mg/mL) is prepared by dissolving lyophilized bovine blood plasma protein (341573; MilliporeSigma) at 37 °C in sterile DPBS without calcium and magnesium. The solution is held at 37 °C for 45 min to allow complete dissolution. The fibrinogen solution is stored in small-volume aliquots at −20 °C for later use. The TG solution (60 mg/mL) is prepared by dissolving lyophilized powder (Moo Glue, TI formula) in DPBS without calcium and magnesium and gently mixing for 20 s. The solution is then placed at 37 °C for 20 min and sterile-filtered immediately before use. A 250 mM $CaCl_2$ stock solution is prepared by dissolving $CaCl_2$ powder in DPBS without calcium and magnesium (Corning); this solution is sterile-filtered and stored at 4 °C in aliquots. To prepare stock solution of thrombin, lyophilized thrombin (Sigma-Aldrich) is reconstituted at 500 U/mL using sterile DPBS and stored at −20 °C in small-volume aliquots. The thrombin aliquots are thawed immediately before use. The rheological and diffusional permeability measurements of the ECM before and after enzymatic cross-linking are described in *SI Appendix*, Figs. S2 and S4. Before casting, an incubation time of ∼15 min is used before quickly mixing this solution with thrombin at a ratio of 500:1 (13). A modified fugitive ink composed of 25 wt % Pluronic F127 (Sigma) and 1 wt % high-molecular-weight PEO (Sigma) is used to print both PT and vascular channels. A 3.5 wt % stock solution is prepared by dissolving powdered PEO (molecular weight 8×10^6 g/mol) in deionized water. A stock solution of 35 wt % Pluronic F127 is homogenized using a Thinky mixer and subsequently stored at 4 °C. The stock solutions are combined and homogenized using a Thinky mixer then sterile-filtered using 0.2-μm filter. A silicone ink composed of a two-part silicone elastomer (SE 1700; Dow Chemical) with a 10:1 base to catalyst (by weight) is used to create customized perfusion chips. It is homogenized using a mixer (AE-310; Thinky Corporation) and printed within 2 h of mixing.

Three-Dimensional Fabrication. All 3D VasPT tissues are housed within a printed silicone gasket on chip. This gasket is produced by loading the silicone ink into a 30-mL syringe, centrifuging to remove air bubbles, and printing through a tapered 410-μm nozzle (EFD, Inc.). The gasket is designed in SolidWorks (Dassault Systemes) and printed onto a 50- × 75-mm glass slide (Corning) using a commercial 3D printer (3D-Bioplotter; EnvisionTEC). The silicone gasket is then cured at 80 °C in a convection oven overnight and stored at room temperature. Next, a thin layer of our modified ECM is cast within printed silicone gasket. This base layer is allowed to dry slightly, allowing it to form a flat surface. The fugitive ink is then printed on this ECM layer using a custom-designed 3D bioprinter equipped with a printhead mounted onto a three-axis, motion-controlled gantry (Aerotech). While the diameter of printed channels can be as small as ∼20 μm, it becomes challenging to seed cells at high density in channels below ∼200 μm in diameter. Immediately after printing, metal pins are pushed through the silicone gasket and brought into contact with the printed ink features. A top layer of ECM is then cast over the printed tubules, nearly filling the gasket. After casting, the ECM is incubated at 37 °C for 2 h. The entire construct is cooled to 4 °C for 15 to 20 min to liquefy the modified fugitive ink, which is then flushed out of the chip using cell media, leaving behind open lumens encapsulated within the modified ECM. To complete their assembly, the chips are placed between a machined stainless-steel base and a thick acrylic lid and screwed into place. Next, sterile two-stop peristaltic tubing (0.25-mm internal diameter; PharMed BPT) is filled with media and connected to the outlet of a sterile filter that is attached to a 10-mL syringe barrel (EFD Nordson) filled with cell media. Silicone tubing is then attached to each inlet and outlet of the chip to form a closed-loop circuit. Clamps are attached to the inlet and outlet tubing of the chip to pinch off the tubing while moving the chip to prevent uncontrolled flow within the tissue construct.

Cell Culture and Seeding. We modified the ATCC protocol to culture human immortalized PTECs (RPTEC/TERT1; ATCC CRL4031). Specifically, we centrifuged the cells at 200 × *g* for 4 min. In addition, the cell suspension is pipetted through a 40-μm strainer to obtain a single-cell suspension for accurate cell count. We also used a modified cell media composed of DMEM F-12 without glucose (pH 7.3 ± 0.05), $NaHCO_3$ (1.2 mg/mL), D-glucose (100 mg/dL), ITS (1× concentration, 13146-5ML; Sigma), triiodothyronine (5 pM), sodium selenite (3.65 ng/mL), PGE1 (25 ng/mL), hydrocortisone (25 ng/mL), ascorbic acid (3.5 μg/mL), and EGF (10 ng/mL). These PTECs were cultured up to passage 20. Human primary GMECs (cAP-0004; Angio-Proteomie) are cultured using the Angio-Proteomie protocol and are used up to passage 8. We seeded PTECs ∼5 d within the 3D VasPT chips before endothelializing the vascular channel. First, each chip is perfused overnight with PTEC media in the incubator before PTEC seeding. Next, 30 μL of the PTEC suspension with a cell density 15×10^6 cells/mL is injected into the printed PT through the outlet using a micropipette. The chip is then placed back into the incubator (37 °C, 5% CO_2) under static conditions for ∼5 h. Perfusion of fresh media is then initiated, and nonadherent cells are flushed out of the PT lumen. Adherent cells cluster and grow until they reach full confluency and circumscribe the lumen (∼3 to 5 d). PTECs are perfused continuously at 3 μL/min, corresponding to a fluidic shear stress 0.3 dynes/cm^2. Media is changed every 2 d. Once the PTECs are confluent, the second reservoir is switched to endothelial cell growth media (EGM2; Lonza) with 1% aprotinin (115 KIU/ml) and 1% anti-anti. The following day GMECs are seeded into the empty vascular lumen following the same procedure for the PTECs and grown to confluency.

Immunostaining, Direct Staining, and Light Microscopy. Immunostaining followed by confocal microscopy is used to characterize the cellular morphology and localization of proteins. Each tissue is fixed for 30 min to 1 h using 10% buffered formalin (Sigma). Samples are washed three times in PBS and blocked overnight using a solution of 2% donkey serum and 1 wt % BSA in PBS. Three-dimensional kidney tissues are then incubated with primary antibodies for 1 d at the dilutions listed in *SI Appendix*, Table S1 in permeabilization buffer (0.5 wt % BSA and 0.125 wt % Triton X-100). The unbound primary antibodies are then removed from the samples by washing them three times in PBS. Samples were then incubated with secondary antibodies using the dilutions listed in *SI Appendix*, Table S1 in a solution of 0.5 wt % BSA and 0.125 wt % Triton X-100 in PBS. Finally, the cells are counterstained with NucBlue and ActinRed for 30 min and then washed for several hours in PBS before imaging. For the hyperglycemia assay, CellROX (C10444; Invitrogen) is used to detect the oxidative stress in live GMECs, and nitrogyrosine antibody is used for further confirmation. Bright-field microscopy is performed using a Nikon Eclipse Ts2 scope equipped with a Zeiss AxioCam MRc 5. Confocal microscopy is performed using an upright Zeiss LSM 710 with water-immersion objectives ranging from 5× to 40×. Image reconstructions of z-stacks are performed in ImageJ or IMARIS.

Electron Microscopy. The 3D VasPT tissues are fixed using 2.5% glutaraldehyde, 1.25% paraformaldehyde, and 0.03% picric acid in 0.1 M sodium cacodylate buffer (pH 7.4) for a minimum of several hours before TEM imaging. The fixative is first perfused through the lumens of the construct, allowing direct exposure to the cell surface, then the constructs are sectioned into small samples (2 × 2 × 2 mm) and immersed in the same fixative. For SEM, the samples are fixed and sectioned following the same protocol. The fixed tissue is then dehydrated with ascending graded ethanol series by subsequent exchanges of dilutions (25, 50, 75, 90, and 100%) in distilled water. The ethanol is removed from the sample using a high-pressure critical point dryer (931 GL; Tousimis). Before imaging, samples were mounted and sputter-coated with a 5-nm layer of platinum–palladium and imaged using Hitachi SU8230 Cold Field Emission SEM.

Quantitative Real-Time PCR. For gene expression analysis, PTECs are isolated from the 3D VasPT tissue by flushing buffer RLT (Qiagen) through the chip and immediately collecting the lysate from the outlet. RNA is purified using the RNeasy mini kit (Qiagen). After RNA purification, cDNA synthesis is performed with the iScript cDNA synthesis kit (Bio-Rad) followed by qPCR using the iTaq Sybr Green Supermix (Bio-Rad) and a CFX96 real-time PCR

machine (Bio-Rad). GAPDH is used as housekeeping gene. Values are calculated by the delta-delta CT method. Primers used for qPCR are described in *SI Appendix*, Table S2.

Permeability Measurements. We measured the barrier function of the epithelium and endothelium within the 3D VasPT models by perfusing cell culture media that contains 25 μg/mL fluorescent Dextran (FITC-Dex, 46945, FD40S, 46946; Sigma) or 25 μg/mL Inulin (F3272; Sigma) through their open lumens and quantifying their diffusional permeability. Each measurement is performed under live cell imaging with both the channels of interest and the surrounding ECM in the field of view (*SI Appendix*, Fig. S9). The diffusion pattern is imaged using a wide-field fluorescent microscope (Zeiss Axio Observer Z1). Diffusional permeability is calculated by quantifying changes in fluorescence intensity over time using $P_d = d(I_2 - I_1)/4t(I_1 - I_b)$ (36), where P_d is the permeability coefficient, I_1 is the mean intensity at initial time point, I_2 is the mean intensity at $t \sim 30$ min, I_b is background intensity, and d is channel diameter.

Albumin and Glucose Reabsorption Studies. In the albumin uptake assay, human serum albumin Cy-5 (HSA-Cy5, Nanocs HS1-S55-1), and inulin-FITC (F3272-1G; Sigma) are perfused through the PT channel (VasPT samples are 10 d postconfluency) with final concentrations 40 μg/mL and 2.5 μg/mL, respectively. Simultaneously, the perfusates from the PT and vasculature outlets are automatically collected (one collection per hour) using a homemade fraction collector. The HSA-Cy5 and inulin-FITC concentrations in the collected perfusate are measured using a microplate reader (Synergy H1 Hybrid Multi-Mode Reader; BioTek). The sample is removed from the incubator after 4 h and placed on a fluorescent microscope (Zeiss Axio Observer Z1) for live imaging at room temperature. The perfusate sample is continuously collected during imaging.

In the glucose reabsorption assay, the glucose level of the media is measured using a commercial glucose meter (Accu-Chek Performa; Roche Diagnostics). The calibration data are reported in *SI Appendix*. The reabsorbed glucose mass is determined by multiplying the glucose level difference arising from reabsorption and half-total media volume. To inhibit the glucose reabsorption in PT, we administered a SGLT-2–specific inhibitor, dapagliflozin (CAS 461432-26-8; Santa Cruz) at a concentration 0.5 μM. Dapagliflozin was administered on day 13 and withdrawn on day 15.

Hyperglycemia Assay and VEGF ELISA. In hyperglycemia experiments, the 3D VasPT samples used are 10 d postconfluency. For control samples, the glucose level of cell media remains unchanged. For the hyperglycemia and hyperglycemia with dapagliflozin administration conditions, the glucose level in the PT channel is increased to 400 mg/dL by adding additional D-glucose to the PTEC media. The administered dapagliflozin concentration is 0.5 μM. After 48 h of perfusion, CellRox 5 μM (C10444; Invitrogen) is perfused through all samples for 30 min. Subsequently, all samples are quickly washed with fresh and warm media and immediately imaged using a confocal microscope.

The level of VEGF-A in the EGM2 is measured using the human VEGF-A ELISA kit (EHVEGFACL; Invitrogen) per the manufacturer's protocol. The VEGF uptake amount is determined by subtracting the VEGF concentration in the perfused media from the initial value (2 ng/mL) of unused EGM2.

Statistical Analysis. Data are reported as mean values ± SDs. Statistical analysis is performed using MATLAB and statistical significance is determined using Tukey's multiple pairwise comparison test. Different significance levels (P values) are indicated with asterisks and specific P values are provided in each figure legend.

ACKNOWLEDGMENTS. We thank Ryuji Morizane, Navin Gupta, Katharina Kroll, Ryan Nagao, Mark Skylar-Scott, and Sebastien Uzel for insightful discussions; Jessica Hermann, Nicole Gampp, Felix Schmitt-Hoffner, Jacquelyn Ho, Koen Breugel, and Don Mau for experiment assistance; Thomas Ferrante, Christine Wang, and Maria Ericsson for imaging assistance; Lori Sanders for videography; and Adrian Roth, Franz Schuler, and Thomas Singer (Roche) for their support of our work. This work was supported by a Roche Postdoctoral Fellowship (to N.Y.C.L.), NIH (Re)Building a Kidney Consortium Grant U01DK107350 (to K.A.H. and J.A.L.), NIH UG3 Grant TR002155 (to N.Y.C.L., K.A.H., and J.A.L.), the Wyss Institute for Biologically Inspired Engineering (D.B.K. and S.S.R.), and a generous donation from GETTYLAB.

1. Eaton D, Pooler J (2004) Vander's Renal Physiology, Lange Physiology Series (Lange Medical Books/McGraw-Hill, New York).
2. Wilmer MJ, et al. (2016) Kidney-on-a-chip technology for drug-induced nephrotoxicity screening. *Trends Biotechnol* 34:156–170.
3. Jang K-J, et al. (2013) Human kidney proximal tubule-on-a-chip for drug transport and nephrotoxicity assessment. *Integr Biol* 5:1119–1129.
4. Meyers CM, Seeff LB, Stehman-Breen CO, Hoofnagle JH (2003) Hepatitis C and renal disease: An update. *Am J Kidney Dis* 42:631–657.
5. Lazzara MJ, Deen WM (2007) Model of albumin reabsorption in the proximal tubule. *Am J Physiol Renal Physiol* 292:F430–F439.
6. Vedula EM, Alonso JL, Arnaout MA, Charest JL (2017) A microfluidic renal proximal tubule with active reabsorptive function. *PLoS One* 12:e0184330.
7. Weber EJ, et al. (2016) Development of a microphysiological model of human kidney proximal tubule function. *Kidney Int* 90:627–637.
8. Jansen J, et al. (2015) Human proximal tubule epithelial cells cultured on hollow fibers: Living membranes that actively transport organic cations. *Sci Rep* 5:16702.
9. Rayner SG, et al. (2018) Reconstructing the human renal vascular-tubular unit in vitro. *Adv Healthc Mater* 7:e1801120.
10. Homan KA, et al. (2016) Bioprinting of 3D convoluted renal proximal tubules on perfusable chips. *Sci Rep* 6:34845.
11. Duckworth W, et al.; VADT Investigators (2009) Glucose control and vascular complications in veterans with type 2 diabetes. *N Engl J Med* 360:129–139.
12. Cooper ME, et al. (1999) Increased renal expression of vascular endothelial growth factor (VEGF) and its receptor VEGFR-2 in experimental diabetes. *Diabetes* 48: 2229–2239.
13. Kolesky DB, Homan KA, Skylar-Scott MA, Lewis JA (2016) Three-dimensional bioprinting of thick vascularized tissues. *Proc Natl Acad Sci USA* 113:3179–3184.
14. Kolesky DB, et al. (2014) 3D bioprinting of vascularized, heterogeneous cell-laden tissue constructs. *Adv Mater* 26:3124–3130.
15. DesRochers TM, Suter L, Roth A, Kaplan DL (2013) Bioengineered 3D human kidney tissue, a platform for the determination of nephrotoxicity. *PLoS One* 8:e59219.
16. Wieser M, et al. (2008) hTERT alone immortalizes epithelial cells of renal proximal tubules without changing their functional characteristics. *Am J Physiol Renal Physiol* 295:F1365–F1375.
17. van Setten PA, et al. (1997) Effects of TNF α on verocytotoxin cytotoxicity in purified human glomerular microvascular endothelial cells. *Kidney Int* 51:1245–1256.
18. Obeidat M, Li L, Ballermann BJ (2014) TIMAP promotes angiogenesis by suppressing PTEN-mediated Akt inhibition in human glomerular endothelial cells. *Am J Physiol Renal Physiol* 307:F623–F633.
19. Yang KS, et al. (2014) Vascular endothelial growth factor-receptor 1 inhibition aggravates diabetic nephropathy through eNOS signaling pathway in db/db mice. *PLoS One* 9:e94540.
20. Pusztaszeri MP, Seelentag W, Bosman FT (2006) Immunohistochemical expression of endothelial markers CD31, CD34, von Willebrand factor, and Fli-1 in normal human tissues. *J Histochem Cytochem* 54:385–395.
21. Daniel E, et al. (2018) Spatiotemporal heterogeneity and patterning of developing renal blood vessels. *Angiogenesis* 21:617–634.
22. Reitsma S, Slaaf DW, Vink H, van Zandvoort MA, oude Egbrink MG (2007) The endothelial glycocalyx: Composition, functions, and visualization. *Pflugers Arch* 454: 345–359.
23. Weinbaum S, Tarbell JM, Damiano ER (2007) The structure and function of the endothelial glycocalyx layer. *Annu Rev Biomed Eng* 9:121–167.
24. Rizzo V, Morton C, DePaola N, Schnitzer JE, Davies PF (2003) Recruitment of endothelial caveolae into mechanotransduction pathways by flow conditioning in vitro. *Am J Physiol Heart Circ Physiol* 285:H1720–H1729.
25. Tasnim F, Zink D (2012) Cross talk between primary human renal tubular cells and endothelial cells in cocultures. *Am J Physiol Renal Physiol* 302:F1055–F1062.
26. Mather A, Pollock C (2011) Glucose handling by the kidney. *Kidney Int Suppl* 79:S1–S6.
27. Birn H, Christensen EI (2006) Renal albumin absorption in physiology and pathology. *Kidney Int* 69:440–449.
28. Lorenz JN, Gruenstein E (1999) A simple, nonradioactive method for evaluating single-nephron filtration rate using FITC-inulin. *Am J Physiol* 276:F172–F177.
29. List JF, Woo V, Morales E, Tang W, Fiedorek FT (2009) Sodium-glucose cotransport inhibition with dapagliflozin in type 2 diabetes. *Diabetes Care* 32:650–657.
30. Meng W, et al. (2008) Discovery of dapagliflozin: A potent, selective renal sodium-dependent glucose cotransporter 2 (SGLT2) inhibitor for the treatment of type 2 diabetes. *J Med Chem* 51:1145–1149.
31. Abdul-Ghani MA, DeFronzo RA, Norton L (2013) Novel hypothesis to explain why SGLT2 inhibitors inhibit only 30-50% of filtered glucose load in humans. *Diabetes* 62: 3324–3328.
32. Patel A, et al.; ADVANCE Collaborative Group (2008) Intensive blood glucose control and vascular outcomes in patients with type 2 diabetes. *N Engl J Med* 358:2560–2572.
33. Ceriello A, dello Russo P, Amstad P, Cerutti P (1996) High glucose induces antioxidant enzymes in human endothelial cells in culture. Evidence linking hyperglycemia and oxidative stress. *Diabetes* 45:471–477.
34. Giugliano D, Ceriello A, Paolisso G (1996) Oxidative stress and diabetic vascular complications. *Diabetes Care* 19:257–267.
35. Ceriello A, et al. (2001) Detection of nitrotyrosine in the diabetic plasma: Evidence of oxidative stress. *Diabetologia* 44:834–838.
36. Price GM, Tien J (2011) Methods for forming human microvascular tubes in vitro and measuring their macromolecular permeability. *Biological Microarrays* (Springer, New York), pp 281–293.